

***LES prediction of wall-pressure
fluctuations and noise of a
low-speed airfoil***

by

**Meng Wang, Stephane Moreau, Gianluca Iaccarino
and Michel Roger**

reprinted from

international journal of



aeroacoustics

volume 8 · number 3 · 2009

published by MULTI-SCIENCE PUBLISHING CO. LTD.,

5 Wates Way, Brentwood, Essex, CM15 9TB UK

E-MAIL: mscience@globalnet.co.uk

WEBSITE: www.multi-science.co.uk

LES prediction of wall-pressure fluctuations and noise of a low-speed airfoil

**Meng Wang^{*}, Stephane Moreau[†], Gianluca Iaccarino[‡]
and Michel Roger[§]**

^{}Department of Aerospace and Mechanical Engineering, University of Notre Dame, Notre Dame, IN 46556, USA, m.wang@nd.edu*

[†]Valeo Thermal Systems, 78321 La Verriere, France, stephane.moreau@valeo.com

[‡]Department of Mechanical Engineering, Stanford University, Stanford, CA 94305, USA, jops@ctr.stanford.edu

[§]Ecole Centrale de Lyon, 36 avenue Guy de Collongue, 69134 Ecully, France, michelroger@ec-lyon.fr

Received February 11, 2008, revision received August 28, 2008, accepted for publication September 15, 2008

ABSTRACT

This paper discusses the prediction of wall-pressure fluctuations and noise of a low-speed flow past a thin cambered airfoil using large-eddy simulation (LES). The results are compared with experimental measurements made in an open-jet anechoic wind-tunnel at Ecole Centrale de Lyon. To account for the effect of the jet on airfoil loading, a Reynolds-averaged Navier-Stokes calculation is first conducted in the full wind-tunnel configuration, and the mean velocities from this calculation are used to define the boundary conditions for the LES in a smaller domain within the potential core of the jet. The LES flow field is characterized by an attached laminar boundary layer on the pressure side of the airfoil and a transitional and turbulent boundary layer on the suction side, in agreement with experimental observations. An analysis of the unsteady surface pressure field shows reasonable agreement with the experiment in terms of frequency spectra and spanwise coherence in the trailing-edge region. In the nose region, characterized by unsteady separation and transition to turbulence, the wall-pressure fluctuations are highly sensitive to small perturbations and thus difficult to predict or measure with certainty. The LES, in combination with the Ffowcs Williams and Hall solution to the Lighthill equation, also predicts well the radiated trailing-edge noise. A finite-chord correction is derived and applied to the noise prediction, which is shown to improve the overall agreement with the experimental sound spectrum.

1. INTRODUCTION

The noise generated by flow over a lifting surface is of major concern in many engineering applications. Examples include propeller noise, rotor noise, wind turbine noise, fan noise, and noise from wings and hydrofoils. Even in the absence of disturbances in the incoming stream, an airfoil (blade) can be noisy due to the unsteady

and turbulent boundary layers and wake generated around the profile and their interaction with it, particularly in the trailing-edge region. This so called self-noise, or trailing-edge noise, is a major contributor to the overall noise in rotating machines and generally defines the lower bound of noise [1].

Trailing-edge noise is much more powerful than the noise radiated by turbulent flows of comparable intensity in free space. This is because when turbulent eddies are convected past the trailing edge, their aeroacoustic source characteristics are modified by the edge, resulting in a more efficient conversion of flow energy to acoustic energy. The theoretical framework for trailing-edge noise has long been established (see, for example, [2, 3, 4, 5]). Ffowcs Williams and Hall [2] employed the acoustic Green's function for a rigid half plane to solve the Lighthill equation [6], and found that acoustic radiation is amplified drastically for turbulent eddies well within one acoustic wavelength from the edge. The far-field sound intensity scales with the fifth power of the characteristic flow velocity, and has a cardioid directivity with maximum in the half plane. The half-plane scattering theory has later been extended by Howe to include the effects of finite chord length [5] and thickness [7] of an airfoil. Howe [5] shows that for an acoustically thin airfoil of finite chord length, the directivity and frequency spectrum of trailing-edge noise deviate from those for a semi-infinite airfoil due to multiple scattering by the leading and trailing edges. The deviation becomes significant at low frequencies, when the wavelength is not small compared to the chord length. He derived an approximate finite-chord Green's function to take account of the multiple scattering effect.

In recent years, aided by the rapid increase in computing power, a number of numerical studies have been performed using Lighthill's theory [6] in conjunction with large-eddy simulation (LES) of the near field [8, 9, 10, 11]. Wang and Moin [8] computed the flow over a model airfoil used by Blake [12] in a trailing-edge experiment at chord Reynolds number of 2.1×10^6 , and obtained reasonable agreement with experimental measurements in terms of velocity and unsteady surface pressure statistics. The acoustic calculation was based on Ffowcs Williams and Hall's solution [2] to the Lighthill equation. However, no acoustic data were available from the same experiment for a quantitative validation. To save computational cost, the simulation was limited to the rear 40% of the airfoil and a spanwise width of just 50% of the airfoil thickness (1.2% chord). In addition, there is uncertainty about the velocity boundary conditions because of wind tunnel installation effects, which can cause the flow to deviate from that in free space [13].

The objective of the present work is to further assess the predictive capability of LES for airfoil self noise. A new experiment was performed at Ecole Centrale de Lyon (ECL) to provide data for comparison with numerical solutions. In the experiment, described in [13, 14, 15], an industrial cambered airfoil (fan blade) was placed at the exit of an open-jet anechoic wind tunnel, as shown in figure 1. The airfoil, designed to achieve low drag by controlling the chordwise diffusion, is known as the controlled diffusion (CD) profile. It has a chord length of 0.1356 m and a span of 0.3 m, and is at an angle of attack of $\alpha = 8^\circ$ measured with respect to the nozzle axis. The reference velocity U_0 and density ρ_0 , taken at the center of nozzle exit, are 16 m/s and 1.25 kg/m³, respectively. Far-field acoustic spectra were measured along with the spatial-

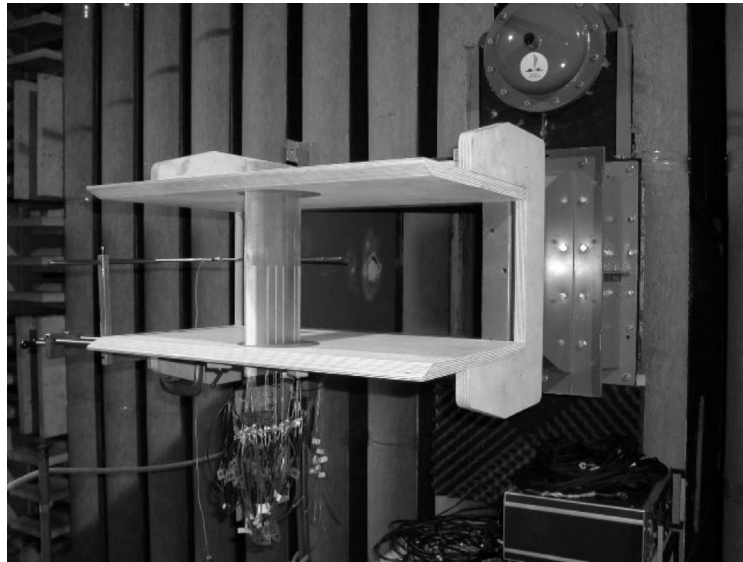


Figure 1: Experimental setup showing an instrumented airfoil mounted in the ECL anechoic open-jet facility.

temporal statistics of surface pressure fluctuations, including the frequency spectra and coherence. The unsteady surface pressure is of interest because it is used to predict the far-field noise in certain aeroacoustic models based on the classical diffraction theory [16, 17, 18]. It can also induce blade vibration which is an additional source of noise. From a fundamental point of view, both the unsteady surface pressure and radiated acoustic pressure are generated by the same velocity source field, and hence an accurate prediction of the surface pressure, particularly near the trailing edge, is indicative of the quality of the flow solution for far-field computation. In this article, we present a validation and analysis of the spatial-temporal statistics of the fluctuating surface pressure field as well as the radiated sound field. The far-field sound spectra are computed using an integral solution to the Lighthill equation with an approximate Green's function. Based on the half-plane Green's function of Ffowcs Williams and Hall [2], a finite-chord correction is applied following the analysis of Howe [5] to account for the effect of multiple scattering by the leading and trailing edges of the airfoil.

The numerical simulation follows closely the experimental flow conditions. The Reynolds number based on chord and maximum nozzle exit velocity is 1.5×10^5 . At this Reynolds number, it is feasible to perform LES with the entire airfoil. Although the details of laminar-to-turbulence transition cannot be captured accurately, the subsequent development of the boundary layer, and hence the trailing-edge noise and surface pressure fluctuations, are relatively insensitive to the transition details as long as the location of the transition is captured approximately. The Mach number based

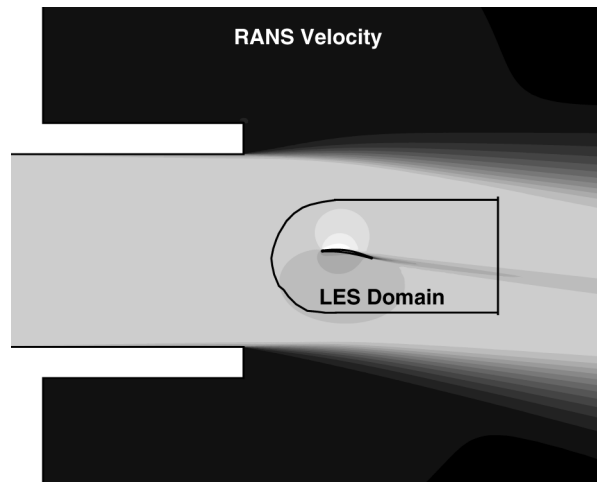


Figure 2: Schematic of LES domain embedded in a RANS solution field. The contours, ranging from -0.04 (dark) to 1.25 (light), indicate the dimensionless streamwise velocity.

on the reference state at nozzle exit is 0.047 , which is sufficiently low to allow the flow field and acoustic source functions to be approximated by incompressible flow solutions.

2. COMPUTATIONAL APPROACH

2.1. Method for flow simulation

It has been shown by Moreau *et al.* [13] that the flow around an airfoil in an open-jet wind tunnel facility differs significantly from that around an isolated airfoil in a uniform stream. In the former case, the airfoil is immersed in a jet of finite width, which is deflected by the circulation created by the airfoil. This can have a large impact on the airfoil loading and its aeroacoustic properties. To account for the effect of jet-airfoil interaction, one possible approach is to include both the jet and airfoil in the simulation. This would, however, make the LES computationally very expensive if not impossible, and add considerable complexity to the problem.

To facilitate the LES while matching closely the experimental conditions, we use an approach which incorporates Reynolds-averaged Navier-Stokes (RANS) solutions into the computation as illustrated in figure 2. First, a RANS simulation is performed in a large computational domain which includes the airfoil, the nozzle and the jet. The velocities obtained from the RANS calculation are used to provide boundary conditions for the LES, performed in a smaller domain embedded in the potential core of the jet. A similar method was employed previously by Wang and Moin [8]. As shown in figure 3, the pressure coefficient from LES is in reasonable agreement with those from the RANS

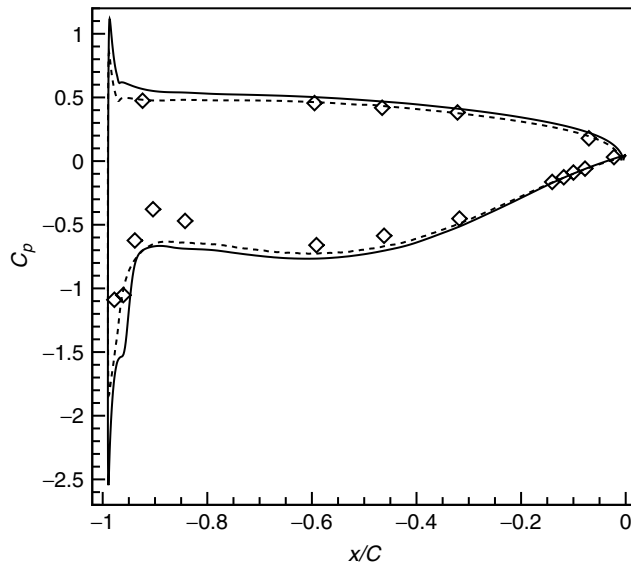


Figure 3: Pressure coefficient along the airfoil surface. —, LES; ----, RANS; \diamond , Experiment.

calculation and experiment, indicating that this approach provides high fidelity in terms of global flow conditions. In order to allow for a reasonably large LES domain within the jet core, the largest nozzle available in the ECL facility was employed. The jet width at the nozzle exit is 50 cm, or 3.69 times the airfoil chord C .

In the LES, we solve the spatially filtered, incompressible Navier-Stokes equations in conjunction with the dynamic subgrid scale model [19, 20] using an energy-conserving, hybrid finite-difference/spectral code described in [8]. The numerical scheme utilizes second-order central differences in the streamwise and cross-stream directions, and Fourier collocation in the spanwise direction. The time advancement is of the fractional step type in combination with the Crank-Nicholson method for viscous terms and third order Runge-Kutta scheme for the convective terms. The Poisson equation for pressure is solved using a multigrid iterative procedure. Simulations are performed on a C -mesh with $960 \times 84 \times 64$ cells, covering a region of size $4C$ (streamwise, x) \times $2.5C$ (cross-stream, y) \times $0.1C$ (spanwise, z). Except in the vicinity of the leading edge, the near-wall grid resolution on the suction side is $\Delta x^+ \leq 34$, $\Delta y^+ \leq 1.1$, and $\Delta z^+ \leq 20$ in wall units, which is adequate for LES. Resolution on the pressure side is considerably coarser because the boundary layer is laminar. The boundary conditions consist of the no-slip condition on the airfoil surface, convective outflow condition in the exit plane, steady RANS velocities along the outer “ C ” boundary, and periodic boundary conditions in the spanwise direction.

2.2. Method for acoustic computation

Given the slender shape of the airfoil (small deviation from the chord relative to the acoustic wavelength), it can be reasonably approximated by a thin plate along its chord for the purpose of acoustic calculations. Furthermore, for acoustic waves that are short compared to the chord length, an approximate Green's function for a rigid half-plane can be employed to solve the Lighthill equation, resulting in the Ffowcs Williams and Hall solution [2]. In the present work the acoustic far field is first computed using a simplified form of the Ffowcs Williams and Hall solution as described in [8]. This solution is derived for a source region well within one acoustic wavelength from the trailing edge, which plays the dominant role in noise generation. The acoustic compactness of the computational domain in the spanwise direction is exploited to simplify the calculation. A detailed discussion of approximations and limitations of this formulation is given in [8]. In the frequency domain the acoustic pressure in the far field is approximately

$$\hat{p}_a(\mathbf{x}, \omega) \approx \frac{e^{i(k|\mathbf{x}| - \frac{\pi}{4})}}{2^{\frac{3}{2}} \pi^{\frac{3}{2}} |\mathbf{x}|} (k \sin \phi)^{\frac{1}{2}} \sin \frac{\theta}{2} \hat{S}(\omega), \quad (1)$$

where

$$S(t) = \int_v \frac{\rho_0}{r_0^{\frac{3}{2}}} \left\{ (u_\theta^2 - u_r^2) \sin \frac{\theta_0}{2} - 2u_r u_\theta \cos \frac{\theta_0}{2} \right\} d^3 \mathbf{y}. \quad (2)$$

In the above equations $\mathbf{x} = (r, \theta, z)$ and $\mathbf{y} = (r_0, \theta_0, z_0)$ represent far-field and source-field positions, respectively, in the cylindrical-polar coordinate system defined in figure 4. Only the velocity components u_r and u_θ , which are normal to the trailing edge, cause amplified scattering sound and thus appear in the source term. The caret denotes temporal Fourier transform, ω is the circular frequency, $k = \omega/c_0$ is the acoustic wavenumber, and $\sin \phi = r/|\mathbf{x}|$.

The half-plane formulation described above is an idealization valid for $kC \gg 1$. In reality, an airfoil of finite chord length is known to cause the acoustic directivity and spectral level to deviate from those of the half-plane due to multiple scattering of acoustic waves. This effect becomes significant at low frequencies. Howe [5] shows that the directivity and spectral level are severely altered when $kC < 10$ and $kC < 2.5$, respectively. To account for the finite-chord effect, an improvement to Eqn 1 is made by using an approximate Green's function for a thin flat plate of finite length C (see figure 4), following the derivations of Howe [5]. As shown in the Appendix, this results in a multiplicative correction factor. The far-field acoustic pressure then reads

$$\hat{p}_a^c(\mathbf{x}, \omega) = \chi \hat{p}_a(\mathbf{x}, \omega), \quad (3)$$

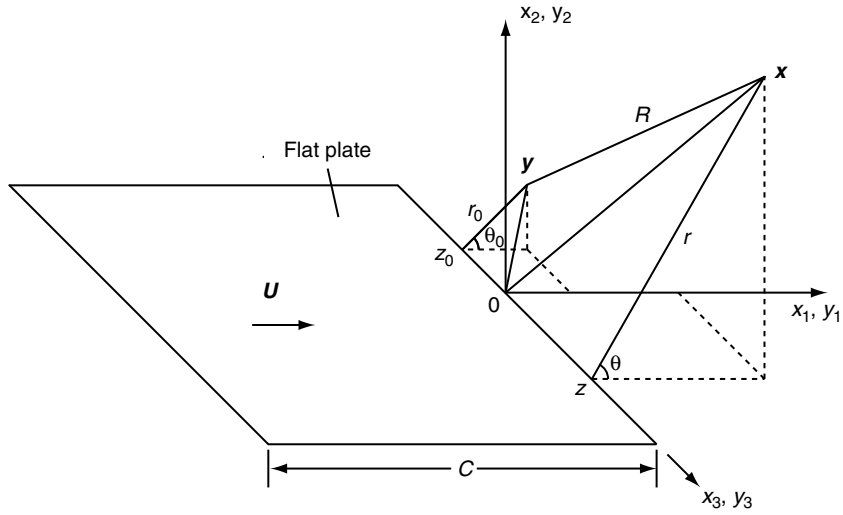


Figure 4: Coordinate system for the finite-chord thin plate used as a model for calculating trailing-edge noise.

where

$$\chi = 1 + \frac{\frac{e^{i\bar{k}}}{\sqrt{\pi\bar{k}}} \mathcal{F}\left(2\sqrt{\frac{\bar{k}}{\pi}} \left|\sin \frac{\theta}{2}\right|\right) - \sqrt{2}e^{-i\frac{\pi}{4}} e^{i\bar{k}\cos\theta} 2\left(\mathcal{F}\sqrt{\frac{\bar{k}}{\pi}} \left|\cos \frac{\theta}{2}\right|\right)}{\left(e^{-i\bar{k}} + \frac{e^{i\bar{k}}}{2\pi i\bar{k}}\right) \sin \frac{\theta}{2}}. \quad (4)$$

In Eqn 4 \mathcal{F} is the Fresnel integral auxiliary function, and $\bar{k} = kC \sin \phi$. At midspan $\left(\phi = \frac{\pi}{2}\right)$ and directly above the airfoil $\left(\theta = \frac{\pi}{2}\right)$, where the acoustic measurement was taken in the experiment, Eqn 4 simplifies to

$$\chi = 1 + 2\mathcal{F}\left(\sqrt{\frac{2kC}{\pi}}\right) \frac{\left(\frac{e^{i\bar{k}C}}{\sqrt{2\pi kC}} - e^{-i\frac{\pi}{4}}\right)}{\left(e^{-i\bar{k}C} + \frac{e^{i\bar{k}C}}{2\pi i\bar{k}C}\right)}. \quad (5)$$

The radiated trailing-edge noise spectra calculated using the above formulations with and without finite-chord correction are presented and compared in Section 3.4.

A more accurate acoustic solution can be obtained by using a Green’s function tailored to the specific airfoil geometry, which needs to be computed numerically [21]. It has been shown in [22] that, for the present airfoil, the use of the “exact” Green’s function does not change the acoustic spectra significantly, and hence the approximate Green’s functions given above are used in the present calculations.

3. RESULTS AND DISCUSSION

3.1. Flow-field characteristics

Figure 5 depicts the iso-contours of the streamwise velocity u/U_0 in a given spanwise plane at a given time instant. It shows a laminar boundary layer on the lower (pressure) side of the airfoil, and a transitional and turbulent boundary layer on the upper (suction) side. Transition on the suction side is triggered by an unsteady laminar separation near the nose, as illustrated clearly in the leading-edge close-up in figure 5. The leading-edge separation is quantitatively identified in figure 6 as a region of negative skin friction coefficient C_f . The streamwise extent of the mean separation bubble is approximately $3.7\%C$. After reattachment the suction side boundary layer evolves downstream into a fully turbulent one. Like its laminar counterpart on the pressure side, the turbulent boundary layer remains attached as it passes the trailing edge despite the strong adverse pressure gradient. There is no coherent vortex shedding at the present angle of attack. These qualitative features of the flow are in agreement with experimental observations.

Figure 7 shows a comparison of the velocity statistics obtained from LES and those from hot-wire measurements at four wake stations (from left to right in each plot): $x/C = 0.0574, 0.0940, 0.1313$ and 0.1686 . The left plot shows the mean streamwise velocity profiles, and the corresponding profiles of the root-mean-square (rms) of streamwise velocity fluctuations are shown on the right. Both quantities are normalized by the free-stream velocity U_∞ . The agreement with experimental data is quite good, although a small upward shift of the wake is observed in the simulation results. Since fluctuating velocities are responsible for wall pressure fluctuations and noise radiation, their accurate computation is a prerequisite for an accurate aeroacoustic prediction.

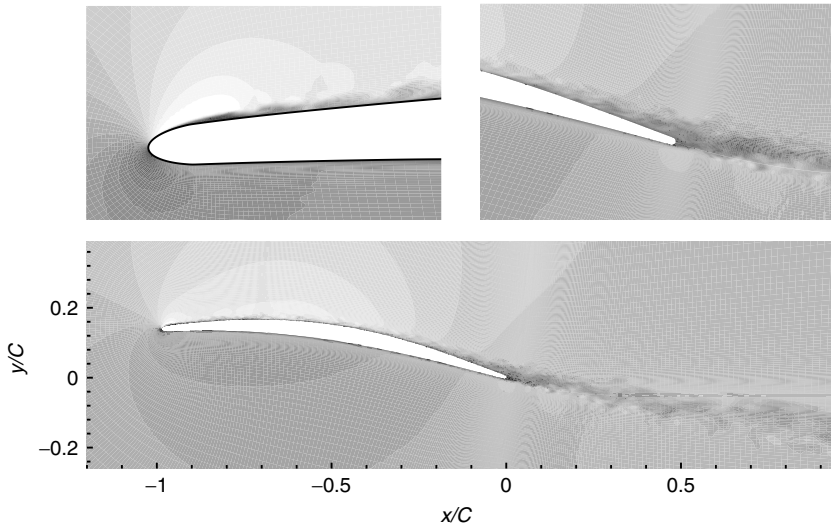


Figure 5: Instantaneous streamwise velocity u/U_0 in a spanwise plane. 25 contour levels ranging from -0.27 (dark) to 1.47 (light) are plotted.

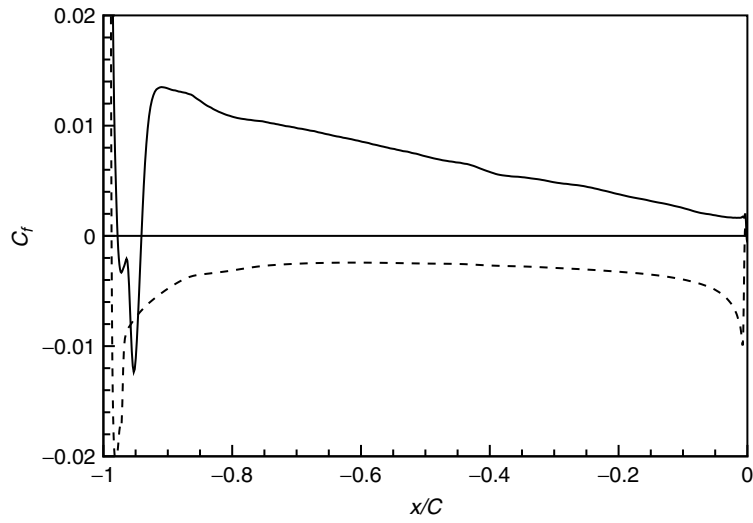


Figure 6: Distribution of skin friction coefficient along the airfoil surface. — , suction side; ---- , pressure side.

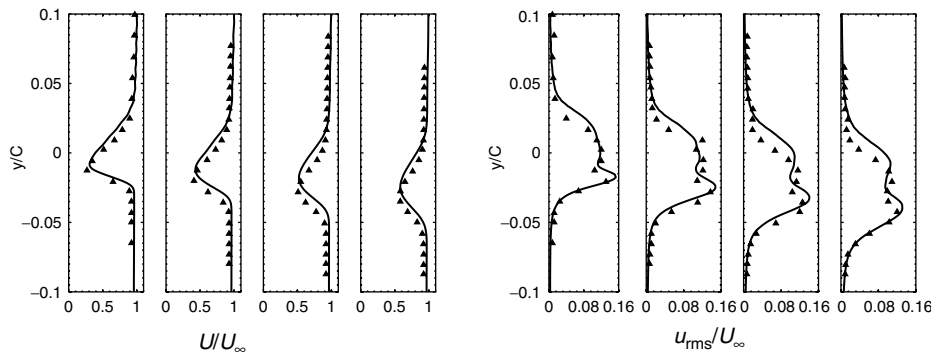


Figure 7: Comparisons of the wake profiles of mean streamwise velocity (left plot) and rms of streamwise velocity fluctuations (right plot) from LES (—) and experiment (\blacktriangle). The four curves in each plot correspond to four wake stations, from left to right, $x/C = 0.0574, 0.0940, 0.1313$ and 0.1686 .

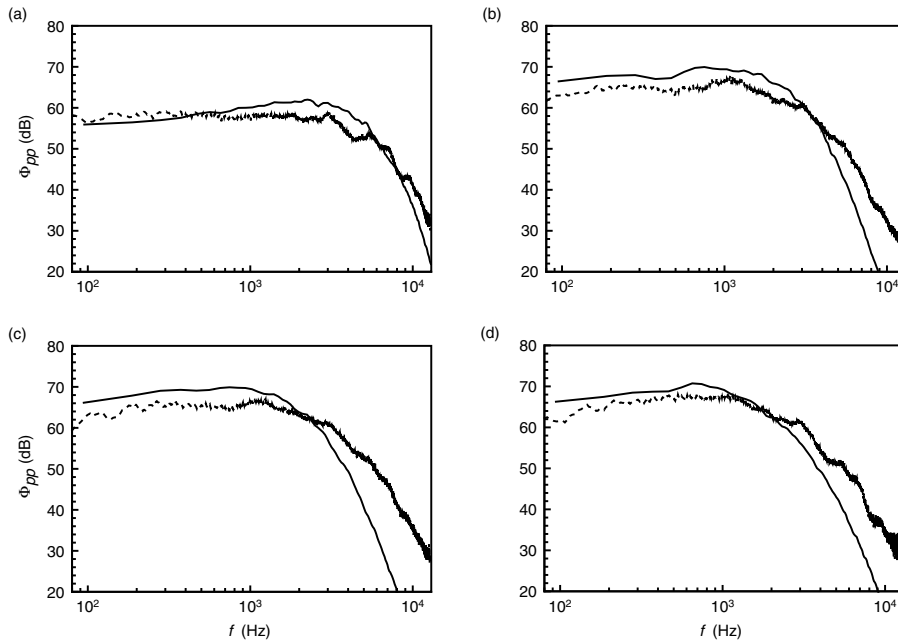


Figure 8: Frequency spectra of pressure fluctuations on the suction side of airfoil surface at (a) $x_c/C = -0.60$, (b) $x_c/C = -0.14$, (c) $x_c/C = -0.08$, and (d) $x_c/C = -0.02$. —, LES; - - - - -, Experiment.

3.2. Frequency spectra of surface pressure fluctuations

The frequency spectra of pressure fluctuations on the suction side of the airfoil surface are shown in figures 8 and 9. To facilitate comparisons with the experimental data, dimensional frequencies (in Hz) and two-sided spectral density (dB per Hz, with reference to 2×10^{-5} Pa) are used. Since the airfoil has an angle of attack, it is convenient to define a chordwise coordinate x_c , which is related to the x -coordinate (cf. figure 5) by $x_c = x/\cos \alpha$, to identify the measurement stations. Along this coordinate the nose is located at $x_c/C = -1$ and the trailing edge is at $x_c/C = 0$.

Plotted in figure 8 are comparisons with experimental measurements at four stations: $x_c/C = -0.60, -0.14, -0.08, -0.02$. The first station (figure 8a) is in the front half of the airfoil. At this location the pressure spectrum already exhibits turbulent boundary layer characteristics and is in good agreement with experimental measurements. Similar spectral shapes are observed at downstream locations. The last three stations shown in figure 8(b-d) are located in the trailing-edge region. Their pressure spectra show overall agreement with the experimental data. In general, LES is seen to overpredict the spectral level by 2 to 4 dBs relative to the experiment in the low to intermediate frequency range. At the high frequency end the LES spectra drop off too rapidly, suggesting that the

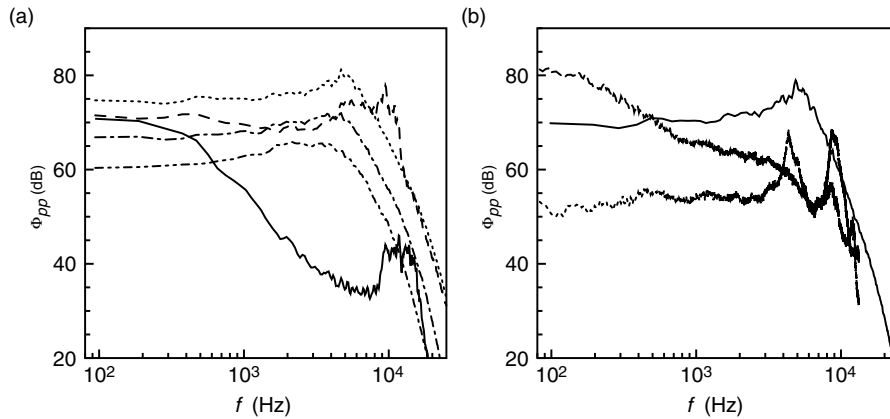


Figure 9: Frequency spectra of pressure fluctuations on the suction surface in the leading-edge area. (a) LES results at five chordwise locations: —, $x_c/C = -0.99$; ----, $x_c/C = -0.97$; ····, $x_c/C = -0.95$; -·-·-, $x_c/C = -0.91$; - - - - , $x_c/C = -0.85$. (b) Comparison with experimental measurements at $x_c/C = -0.95$: —, LES; ----, measurement 1; ·····, measurement 2.

boundary layer lacks very small scale structures. This is not atypical of LES predictions (e.g. [8, 23]), although somewhat surprising given the good grid resolution employed in the computation and the fact that high frequency contents are much better captured at the upstream location shown in figure 8a.

A useful observation from figure 8(b–d) is that the pressure spectra exhibit only small variations in the trailing-edge region (within the last 15% chord). This is important for the aeroacoustic prediction models based on pressure diffraction theory (e.g. [16, 17, 18]), which utilize the frequency spectrum of wall pressure at a single point near the trailing edge as an input. The precise location is arbitrary as long as the spectrum is not affected by edge diffraction. This approach necessarily requires the boundary layer to be self-similar so that the wall pressure spectrum does not exhibit strong sensitivity to the streamwise position. The spectra obtained for the present flow exhibit this property despite the adverse pressure gradient, indicating that this modeling approach is suitable for the far-field noise prediction. Note that the underprediction of the wall-pressure spectra at high frequencies does not necessarily indicate a serious problem for noise prediction, since the high-frequency portion of the source spectrum is an inefficient radiator of noise. However, this issue cannot be addressed fully because the acoustic measurements, to be presented in Section 3.4, do not cover frequencies beyond 2 kHz.

In contrast to the trailing-edge area, the pressure spectrum in the leading-edge region shows extremely strong dependence on position. Figure 9a depicts the frequency spectra at locations $x_c/C = -0.99, -0.97, -0.95, -0.91,$ and -0.85 . The first station is upstream of the unsteady separation, and hence the spectrum lacks high frequency

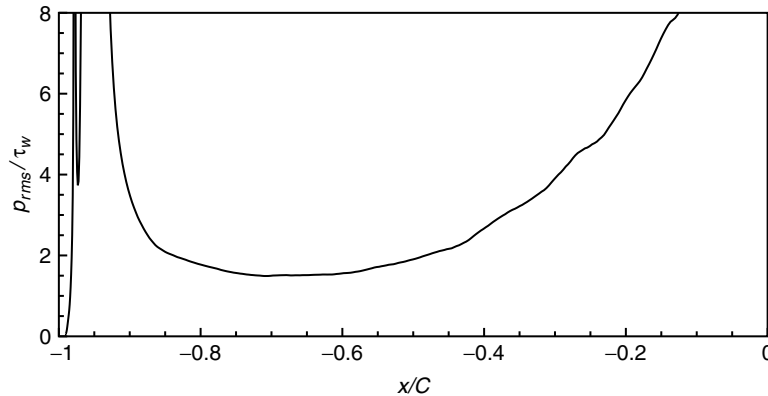


Figure 10: Variation of p_{rms}/τ_w along the airfoil suction surface, computed using LES.

contents. The second station is inside the separation, and the other three are downstream of reattachment. The spectral levels are highly elevated inside the separation and immediately following the reattachment as a result of the shear layer motions and laminar breakdown. It should be pointed out that the detailed transition process, including the precise locations of separation and reattachment, is strongly dependent on incoming flow disturbances. No free-stream turbulence is provided in the computation, whereas in the experiment, the residual turbulence level in the incident flow is approximately 0.8% of the mean velocity. The experimental pressure spectra in the leading-edge region show significant variations from one measurement to another. As an example, two sets of measurements at the same location, $x/C = -0.95$, are plotted in figure 9b along with the LES solution. The discrepancies among the three curves are very large. An accurate simulation of the leading-edge region would require a precise characterization of the incoming turbulence as well as very accurate numerics. However, given the non-repeatability even among experimental measurements, such a task may prove very challenging.

The rms value of pressure fluctuations p_{rms} , normalized by the local mean wall shear stress τ_w , is plotted in figure 10 along the suction surface. The curve is truncated in the nose and trailing-edge regions because of the exceedingly small τ_w values caused by flow separation and adverse pressure gradient. In the region $-0.8 \leq x/C \leq -0.4$, the pressure gradient is nearly zero (cf. figure 3), and p_{rms}/τ_w varies from 1.5 to 2.7. This is consistent with previous numerical and experimental values for equilibrium turbulent boundary layers at similar low Reynolds numbers (e.g. [24]).

3.3. Correlation and coherence

The evolution of the spatial and temporal scales in the turbulent boundary layer is reflected in the space-time correlation of the fluctuating surface pressure, depicted in figure 11 as a function of temporal and spanwise spatial separations at four streamwise

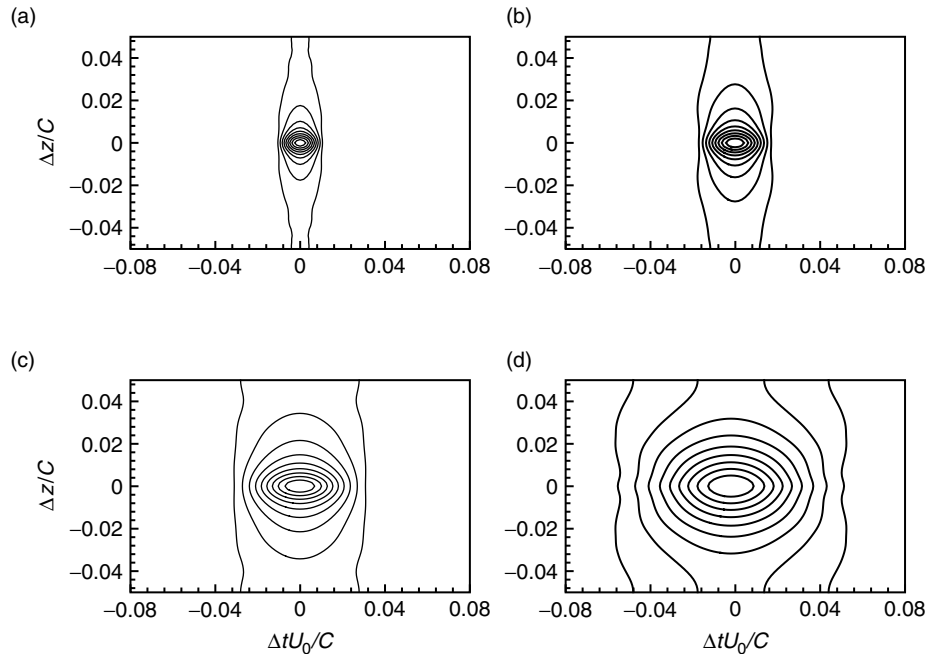


Figure 11: Contours of space-time correlation of the fluctuating pressure on the suction surface as a function of spanwise and temporal separations, at streamwise locations (a) $x_c/C = -0.60$, (b) $x_c/C = -0.23$, (c) $x_c/C = -0.02$, and (d) $x_c/C = 0$ (trailing edge). Contour levels are from 0.1 to 0.9, with increment 0.1.

locations $x_c/C = -0.60, -0.23, -0.02$, and 0. A significant growth of the spanwise and temporal scales is observed from the first station to the third, as a result of a thickening boundary layer caused by the adverse pressure gradient. A similar growth in streamwise correlation scales can be inferred from the temporal scales through Taylor's hypothesis. The last station, $x_c/C = 0$, is in the back of the trailing edge, which is blunt on a small scale (see figure 5). The correlation spatial and temporal scales at this location (figure 11d) are found to be much larger than those of its close neighbor, $x_c/C = -0.02$ (figure 11c). Note that the spanwise correlation coefficient in figure 11 decays to between 0.1 and 0.2 over a maximum separation equal to one half of the periodic spanwise domain size. This is, while not ideal, considered reasonable for this flow and much better than in some related studies (e.g. [8]). To test the sensitivity of the correlation to spanwise domain size, a separate simulation with twice the spanwise domain size but coarser grid resolution has been conducted. The results show only a marginal improvement, and the minimum spanwise correlation remains larger than 0.1.

An important parameter in trailing-edge noise prediction (both modeling and computation) is the coherence length scale of the source field in the spanwise direction, since it represents the size of a source region which radiates independently from sources

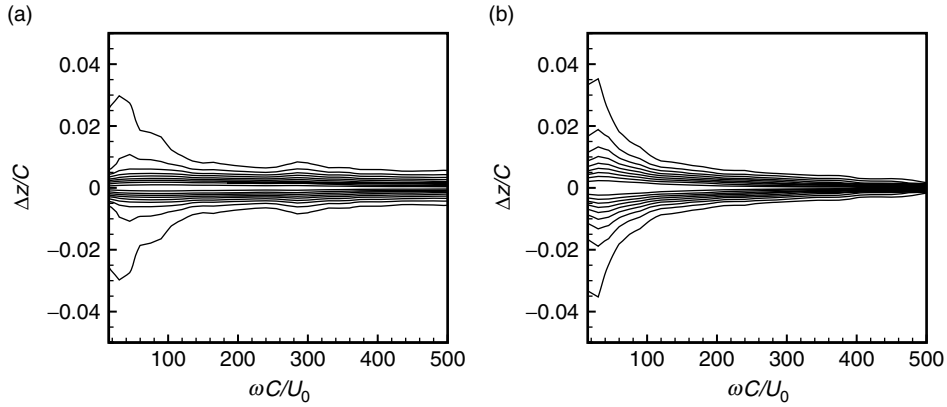


Figure 12: Contours of spanwise coherence of the fluctuating pressure on the suction surface as a function of frequency and spanwise separation, at streamwise locations (a) $x_c/C = -0.60$ and (b) $x_c/C = -0.02$. Contour levels are from 0.1 to 0.9, with increment 0.1.

in neighboring regions in a statistical sense. The coherence is essentially the two-point correlation coefficient in the frequency domain, defined as

$$\gamma^2(\mathbf{x}, \mathbf{r}, \omega) = \frac{|\Phi_{pp}(\mathbf{x}, \mathbf{r}, \omega)|^2}{|\Phi_{pp}(\mathbf{x}, 0, \omega)| |\Phi_{pp}(\mathbf{x} + \mathbf{r}, 0, \omega)|}, \quad (6)$$

where the cross spectrum function Φ_{pp} is the Fourier transform of the space-time cross correlation function

$$\Phi_{pp}(\mathbf{x}, \mathbf{r}, \omega) = \int_{-\infty}^{\infty} \langle p(\mathbf{x}, t) p(\mathbf{x} + \mathbf{r}, t + \tau) \rangle e^{-i\omega\tau} d\tau. \quad (7)$$

Figure 12 shows the surface pressure coherence as a function of spanwise separation and frequency, at locations $x_c/C = -0.60$ and -0.02 . These two contour plots should be contrasted with the corresponding correlation plots in figure 11a and figure 11c, respectively. It is observed that the increased spanwise correlation near the trailing edge is a low frequency effect. The higher frequency components near the trailing edge are in fact less correlated (having smaller coherence length) than their upstream counterparts.

In figure 13a, a comparison is made between the experimental and computed values of the spanwise coherence of fluctuating surface pressure at the near trailing-edge point $x_c/C = -0.02$. Two spanwise separations, $\Delta z/C = 0.02$ and 0.04 , are considered. The LES results are shown to predict the correct values and frequency-variations of the

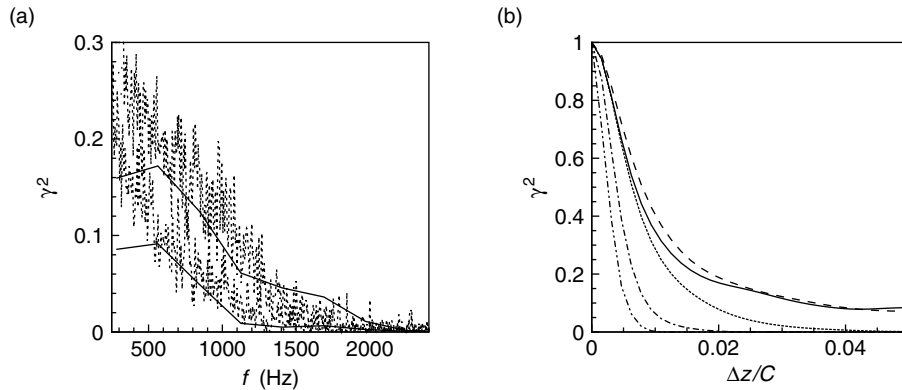


Figure 13: Spanwise coherence of fluctuating pressure on the suction surface at $x_c/C = -0.02$. (a) Coherence plotted against frequency in Hz: —, LES; ····, experiment. Upper curves are for spanwise separation $\Delta z/C = 0.02$, and lower curves are for $\Delta z/C = 0.04$. (b) Coherence plotted against spanwise separation: —, $\omega C/U_0 = 15$ (281 Hz); ----, $\omega C/U_0 = 30$ (563 Hz); ····, $\omega C/U_0 = 60$ (1126 Hz); - · - ·, $\omega C/U_0 = 120$ (2252 Hz); - - - -, $\omega C/U_0 = 240$ (4503 Hz).

coherence in both cases except at the low frequency end ($f < 500$ Hz). It appears that the coherence at low frequencies, particularly for relatively large separations as measured in the experiment, is extremely sensitive to sample size and numerical errors. In figure 13b the coherence at the same location is plotted as a function of spanwise separation for five discrete frequencies. The rapid decay of the coherence with spanwise separation, even at low frequencies (see also figure 12), indicates that the current spanwise computational domain size allows the capturing of a statistically independent acoustic source region and the computation of coherence length scales; both are key to the computation of radiated noise. However, the accuracy of the lower frequency coherence needs to be improved.

3.4. Radiated noise

The radiated sound field is computed following the method described in Section 2.2. The source term in Eqn 2 is evaluated at every four time steps in the LES using the velocities obtained from LES. The sampling resolution $\Delta t_s U_0 / C \approx 1.64 \times 10^{-3}$. The total record of $N = 3584$ time samples, covering a period $T_s U_0 / C \approx 5.88$, is divided into 13 segments with a 50% overlap. For each segment, Eqns 1, 3 and 5 are used to compute the acoustic pressure with infinite and finite chord approximations. The sound spectra are then calculated from the frequency-domain sound pressure and averaged over 13 segments.

Since the spanwise domain size in the LES is only $0.1C$ while the airfoil span in the experiment is approximately $2.21C$, the total sound spectrum is calculated as the sum

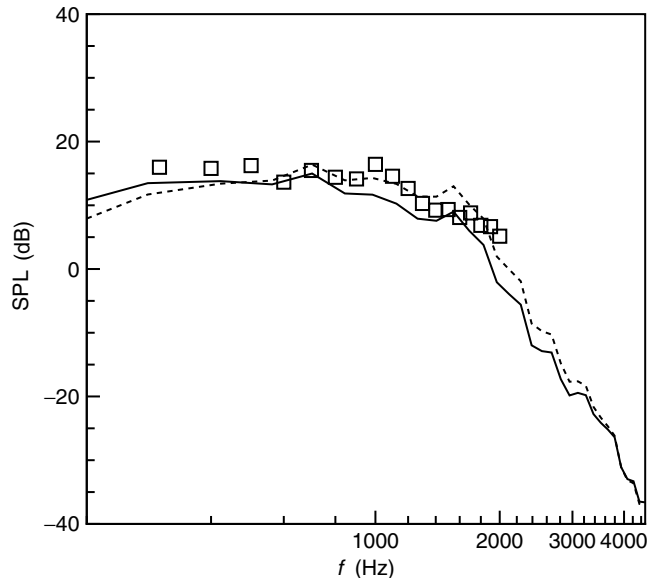


Figure 14: Sound pressure levels in dB (integrated over 8 Hz bin width and with reference to 2×10^{-5} Pa) in the mid-span plane 2 m above the airfoil trailing edge ($r = 2$ m, $\theta = 90^\circ$). —, computed with half-plane Green's function; - - -, computed with finite-chord correction; \square , experiment.

of contributions from $2.21C/0.1C = 22.1$ independent sources. This is justified because, based on the results in figures 12 and 13, the spanwise coherence length of the surface pressure is smaller than the computational domain size at nearly all frequencies.

Figure 14 compares the numerical predictions of the sound pressure spectra with the ECL measurement in the mid-span plane two meters above the airfoil trailing edge, i.e., at $r = 2$ m and $\theta = 90^\circ$. The sound pressure levels (SPLs), plotted as a function of frequency in Hz, have been integrated over an 8 Hz bin width and are with reference to 2×10^{-5} Pa. A favorable agreement is observed over the entire measured frequency range of up to 2000 Hz. The higher frequency portion of the spectrum cannot be verified due to lack of experimental data.

The effect of the finite chord on the computed noise spectrum is noticeable in figure 14. Similar to what was found with the extended Amiet's model [18], the finite chord has an impact at frequencies below approximately 3000 Hz, yielding lower SPLs below 500 Hz and higher SPLs above that frequency, with a peak difference of up to 4 dB at approximately 1500 Hz. Except at the low frequency end, the overall agreement with experimental data is improved by the finite-chord correction.

It should be pointed out that the results in figure 14, based on a single observer location, do not provide a comprehensive comparison between the half-plane and finite-chord models. A major impact of the finite-chord correction is on the acoustic directivity. Howe [5] shows that using the approximate finite-chord Green's function

provides a uniformly valid description of the directivity, ranging from the compact dipole type at low frequencies ($kC \ll 1$) to the cardioid shape at high frequencies ($kC \gg 1$). Multiple lobes arise in the directivity pattern due to repeated scattering of waves by the trailing and leading edges. In contrast, a cardioid directivity is obtained for all frequencies if the half-plane Green's function is employed. This difference in directivity is also accounted for by the finite-chord correction factor given in Eqn. 4.

4. CONCLUSIONS

This work describes a systematic validation of an LES based methodology for predicting the space-time characteristics of the fluctuating pressure on a thin, cambered airfoil at 8° angle of attack and the airfoil self-noise emitted from the trailing-edge region. The computational results are compared with experimental measurements carried out at ECL in terms of wake velocity statistics, frequency spectra and spanwise coherence of the surface pressure fluctuations, and the far-field sound spectra. The relatively low Reynolds number of 1.5×10^5 based on chord allows the simulation to be performed with the entire airfoil in the computational domain. Transition is triggered naturally by unsteady laminar separation near the nose.

To replicate faithfully the experimental flow conditions in the simulation, a RANS calculation is first performed in an open-jet wind tunnel configuration. The resulting velocity profiles are then used to define the boundary conditions for LES in a smaller, C -mesh domain within the potential core of the jet. This approach is shown to provide the correct global flow condition in terms of airfoil loading. The precise turbulent inflow condition, which can affect the leading-edge transition, is not prescribed. It is found that the pressure spectrum beneath the fully developed turbulent boundary layer is insensitive to the details of the upstream transition process, as long as the location of the transition is captured approximately.

The LES flow field is characterized by an attached laminar boundary layer on the pressure side of the airfoil and a transitional and turbulent boundary layer on the suction side, in agreement with experimental observations. A spectral analysis of the fluctuating surface pressure field shows reasonable agreement with experimental values in the mid- and aft-sections of the airfoil. In the nose region, characterized by unsteady separation and transition, the flow and wall-pressure fluctuations are highly sensitive to small inflow perturbations. Their spatial-temporal statistics are difficult to measure experimentally or predict computationally with certainty. LES is also shown to predict the spanwise coherence of the surface pressure field to reasonable satisfaction compared with the experiment except at the low frequency end. In addition to the validation study using experimental data, an analysis of the spatial and temporal structures of the unsteady pressure field and their evolution has been carried out.

The radiated trailing-edge noise is computed using acoustic source functions extracted from the LES data in the framework of Lighthill's aeroacoustic theory. The Ffowcs William and Hall solution, which is based on the half-plane Green's function, is employed with a finite-chord correction following Howe's approximation to account for the multiple scattering by the leading and trailing edges of the airfoil. The method is shown to predict well the far-field sound pressure spectra. Although the effect of

finite-chord correction is relatively small, it improves the overall agreement with experimental data.

ACKNOWLEDGMENTS

The simulations reported in this paper were performed when the first author was at the Center for Turbulent Research, Stanford University/NASA Ames Research Center with support from ONR Grant N00014-01-1-0423. Additional support was provided by ONR Grant N00014-06-1-0640. We gratefully acknowledge Douglas Neal of Michigan State University for providing the experimental wake velocity data, and Parviz Moin of Stanford University for useful discussions.

REFERENCES

- [1] Wright, S. E., The Acoustic Spectrum of Axial Flow Machines, *Journal of Sound and Vibration*, 1976, 45(2), 165–223.
- [2] Ffowcs Williams, J. E. and Hall, L. H., Aerodynamic Sound Generation by Turbulent Flow in the Vicinity of a Scattering Half Plane, *Journal of Fluid Mechanics*, 1970, 40, 657–670.
- [3] Crighton, D. G. and Leppington, F. G., On the Scattering of Aerodynamic Noise, *Journal of Fluid Mechanics*, 1971, 46, 577–597.
- [4] Howe, M. S., A Review of the Theory of Trailing Edge Noise, *Journal of Sound and Vibration*, 1978, 61(3), 437–465.
- [5] Howe, M. S., Edge-Source Acoustic Green's Function for an Airfoil of Arbitrary Chord, with Application to Trailing-Edge Noise, *The Quarterly Journal of Mechanics and Applied Mathematics*, 2001, 54(1), 139–155.
- [6] Lighthill, M. J., On Sound Generated Aerodynamically; I. General Theory, *Proceedings of the Royal Society of London, Series A: Mathematical and Physical Sciences*, 1952, 211(1107), 564–587.
- [7] Howe, M. S., Trailing Edge Noise at Low Mach Numbers, *Journal of Sound and Vibration*, 1999, 225(2), 211–238.
- [8] Wang, M. and Moin, P., Computation of Trailing-Edge Flow and Noise Using Large-Eddy Simulation, *AIAA Journal*, 2000, 38(12), 2201–2209.
- [9] Manoha, E., Troff, B. and Sagaut, P., Trailing-Edge Noise Prediction Using Large-Eddy Simulation and Acoustic Analogy, *AIAA Journal*, 2000, 38(4), 575–583.
- [10] Oberai, A. A., Rognaldin F. and Hughes, T. J. R., Computation of Trailing-Edge Noise due to Turbulent Flow over an Airfoil, *AIAA Journal*, 2002, 40(11), 2206–2216.
- [11] Wang, M., Marsden, A. L. and Moin, P., Computation and Control of Trailing-Edge Noise, in *Proceedings of the 26th Symposium on Naval Hydrodynamics, Vol. III*, Rome, Italy, Sept. 17-22, 2006, 169–182.

- [12] Blake, W. K., *A Statistical Description of Pressure and Velocity Fields at the Trailing Edge of a Flat Strut*, DTNSRDC Report 4241, David Taylor Naval Ship R & D Center, Bethesda, Maryland, 1975.
- [13] Moreau, S., Henner, M., Iaccarino, G., Wang, M. and Roger, M., Analysis of Flow Conditions in Free-Jet Experiments for Studying Airfoil Self-Noise, *AIAA Journal*, 2003, 41(10), 1895–1905.
- [14] Roger, M. and Moreau, S., Broadband Self-Noise from Loaded Fan Blades, *AIAA Journal*, 2004, 42(3), 536–544.
- [15] Moreau, S. and Roger, M., Effect of Airfoil Aerodynamic Loading on Trailing-Edge Noise Sources, *AIAA Journal*, 2005, 43(1), 41–52.
- [16] Amiet, R. K., Noise due to Turbulent Flow Past a Trailing Edge, *Journal of Sound and Vibration*, 1976, 47(3), 387–393.
- [17] Brooks, T. F. and Hodgson, T. H., Trailing Edge Noise Prediction from Measured Surface Pressures, *Journal of Sound and Vibration*, 1981, 78(1), 69–117.
- [18] Roger, M. and Moreau, S., Back-Scattering Correction and Further Extensions of Amiet’s Trailing-Edge Noise Model. Part I: Theory, *Journal of Sound and Vibration*, 2004, 286(3), 477–506.
- [19] Germano, M., Piomelli, U., Moin, P. and Cabot, W. H., A Dynamic Subgrid-Scale Eddy Viscosity Model, *Physics of Fluids A*, 1991, 3(7), 1760–1765.
- [20] Lilly, D. K., A Proposed Modification of the Germano Subgrid Scale Closure Method, *Physics of Fluids A*, 1992, 4(3), 633–635.
- [21] Wang, M., Freund, J. B. and Lele, S. K., Computational Prediction of Flow-Generated Sound, *Annual Review of Fluid Mechanics*, 2006, 38, 483–512.
- [22] Moreau, S., Neal, D., Khalighi, Y., Wang, M. and Iaccarino, G., Validation of Unstructured-Mesh LES of the Trailing-Edge Flow and Noise of a Controlled-Diffusion Airfoil, in *Proceedings of the 2006 Summer Program*, Center for Turbulence Research, Stanford University/NASA Ames Research Center, 2006, 533–546.
- [23] Wang, M. and Moin, P., Dynamic Wall Modeling for Large-Eddy Simulation of Complex Turbulent Flows, *Physics of Fluids*, 2002, 14(7), 2043–2051.
- [24] Choi, H. and Moin, P., On the Space-Time Characteristics of Wall-Pressure Fluctuations, *Physics of Fluids A*, 1990, 2(8), 1450–1460.
- [25] Howe, M. S., *Acoustics of Fluid-Structure Interactions*, Cambridge University Press, Cambridge, 1999.

APPENDIX: FINITE CHORD CORRECTION

In this appendix a finite-chord correction to the Ffowcs Williams and Hall solution to the Lighthill equation, as represented in Eqns 1 and 2, is derived following the multiple scattering analysis of Howe [5].

Starting from Lighthill's equation, Ffowcs Williams and Hall obtained the following expression in the cylindrical coordinates defined in figure 4 for the acoustic pressure [2]:

$$\begin{aligned}
 \hat{p}_a(\mathbf{x}, \omega) = & - \int_V \rho_0 \left\{ \widehat{u_r^2} \frac{\partial^2 G}{\partial r_0^2} + \widehat{u_z^2} \frac{\partial^2 G}{\partial z_0^2} + \widehat{u_r u_z} \left[\frac{\partial}{\partial r_0} \left(\frac{\partial G}{\partial z_0} \right) + \frac{\partial}{\partial z_0} \left(\frac{\partial G}{\partial r_0} \right) \right] \right. \\
 & + \widehat{u_r u_\theta} \left[\frac{\partial}{\partial r_0} \left(\frac{1}{r_0} \frac{\partial G}{\partial \theta_0} \right) + \frac{1}{r_0} \frac{\partial}{\partial \theta_0} \left(\frac{\partial G}{\partial r_0} \right) - \frac{1}{r_0^2} \frac{\partial G}{\partial \theta_0} \right] \\
 & + \widehat{u_\theta u_z} \left[\frac{1}{r_0} \frac{\partial}{\partial \theta_0} \left(\frac{\partial G}{\partial z_0} \right) + \frac{\partial}{\partial z_0} \left(\frac{1}{r_0} \frac{\partial G}{\partial \theta_0} \right) \right] \\
 & \left. + \widehat{u_\theta^2} \left[\frac{1}{r_0^2} \frac{\partial^2 G}{\partial \theta_0^2} + \frac{1}{r_0} \frac{\partial G}{\partial r_0} \right] \right\} d^3 \mathbf{y},
 \end{aligned} \tag{8}$$

where u_r , u_θ , and u_z are the three velocity components, the caret denotes Fourier frequency transform, and G is the Green's function in the frequency domain. Note that in the second line, an erroneous factor of 2 in the second term inside the square brackets found in the original equation has been removed. Ffowcs Williams and Hall employed the half-plane Green's function to derive an expression for the far-field acoustic pressure, which simplifies to Eqns 1 and 2 for a source region that is well within one acoustic wavelength from the trailing edge ($kr_0 \ll 1$) and is acoustically compact in the spanwise direction.

Recently, Howe [5] derived a more general Green's function to account for the multiple scattering at the leading and trailing edges of an airfoil in the framework of Howe's analogy [25]. In his analysis the far-field scattering Green's function for finite chord is written as

$$G(\mathbf{x}, \mathbf{y}, \omega) = G_1(\mathbf{x}, \mathbf{y}, \omega) + G_{LE}(\mathbf{x}, \mathbf{y}, \omega) + G_{TE}(\mathbf{x}, \mathbf{y}, \omega), \tag{9}$$

where

$$G_1(\mathbf{x}, \mathbf{y}, \omega) = \frac{e^{ik|\mathbf{x}|}}{4\pi |\mathbf{x}|} \left(\frac{2e^{-i\frac{\pi}{4}}}{\sqrt{\pi}} \sqrt{2kr_0 \sin \phi} \sin \frac{\theta}{2} \sin \frac{\theta_0}{2} \right) \equiv \alpha \sqrt{r_0} \sin \frac{\theta_0}{2} \tag{10}$$

is the scattering part of the half-plane Green's function which provides the leading approximation to the edge scattering noise. Here and in subsequent derivations we adopt Howe's definition of the Green's function except for an opposite sign. Additional contributions to G due to multiple scattering at the airfoil leading and trailing edges can be approximated by, according to Howe [5],

$$\begin{aligned}
 G_{LE}(\mathbf{x}, \mathbf{y}, \omega) &= -\frac{\sqrt{kr_0} \sin \phi \sin \frac{\theta_0}{2} e^{ik(\mathbf{x}\mathbf{l} + C \sin \phi (1 + \cos \theta))}}{i\pi^{\frac{3}{2}} |\mathbf{x}| \left(1 + \frac{e^{i2kC \sin \phi}}{2\pi i k C \sin \phi}\right)} \mathcal{F}\left(2\sqrt{\frac{kC \sin \phi \cos^2 \frac{\theta}{2}}{\pi}}\right) \\
 &\equiv \beta \sqrt{r_0} \sin \frac{\theta_0}{2},
 \end{aligned} \tag{11}$$

$$\begin{aligned}
 G_{TE}(\mathbf{x}, \mathbf{y}, \omega) &= \frac{\sqrt{r_0} \sin \frac{\theta_0}{2} e^{ik(\mathbf{x}\mathbf{l} + 2C \sin \phi)}}{\sqrt{2iC} \pi^2 |\mathbf{x}| \left(1 + \frac{e^{i2kC \sin \phi}}{2\pi i k C \sin \phi}\right)} \mathcal{F}\left(2\sqrt{\frac{kC \sin \phi \sin^2 \frac{\theta}{2}}{\pi}}\right) \\
 &\equiv \gamma \sqrt{r_0} \sin \frac{\theta_0}{2},
 \end{aligned} \tag{12}$$

where \mathcal{F} is the Fresnel integral auxiliary function. Substituting Eqn 10 into Eqn 8, and noting that only derivatives with respect to r_0 and θ_0 cause amplified edge sound, we obtain a leading approximation

$$\hat{p}_a(\mathbf{x}, \omega) = \frac{\alpha}{4} \int_V \frac{\rho_0}{r_0^{\frac{3}{2}}} \left[(\widehat{u_\theta^2} - \widehat{u_r^2}) \sin \frac{\theta_0}{2} - 2\widehat{u_r u_\theta} \cos \frac{\theta_0}{2} \right] d^3 \mathbf{y} = \frac{\alpha}{4} \hat{S}(\omega), \tag{13}$$

valid for $kr_0 \ll 1$ and $kz_0 \ll 1$ [8]. This is the origin of Eqns 1 and 2. Since G_{LE} and G_{TE} have the same functional dependence on r_0 and θ_0 as G_1 , following the same derivation, their contributions to the far-field acoustic pressure are $\frac{\beta}{4} \hat{S}(\omega)$ and $\frac{\gamma}{4} \hat{S}(\omega)$, respectively. The acoustic pressure corrected for the finite-chord effect is then

$$\hat{p}_a^c(\mathbf{x}, \omega) = \frac{\alpha + \beta + \gamma}{4} \hat{S}(\omega) = \left(1 + \frac{\beta + \gamma}{\alpha}\right) \hat{p}_a. \tag{14}$$

Based on the definitions of α , β and γ in Eqns 10–12, the finite-chord correction factor is

$$1 + \frac{\beta + \gamma}{\alpha} = 1 + \frac{\frac{e^{i\bar{k}}}{\sqrt{\pi \bar{k}}} \mathcal{F}\left(2\sqrt{\frac{\bar{k}}{\pi}} \left|\sin \frac{\theta}{2}\right|\right) - \sqrt{2} e^{-i\frac{\pi}{4}} e^{i\bar{k} \cos \theta} \mathcal{F}\left(2\sqrt{\frac{\bar{k}}{\pi}} \left|\cos \frac{\theta}{2}\right|\right)}{\left(e^{-i\bar{k}} + \frac{e^{i\bar{k}}}{2\pi i \bar{k}}\right) \sin \frac{\theta}{2}}, \tag{15}$$

where $\bar{k} = kC \sin \phi$.

